$A_2B_{n-1}Pb_nI_{3n+1}$ (A = BA, PEA; B = MA, n = 1, 2): Engineering Quantum-well Crystals for High Mass Density and Fast Scintillators

Md Abdul Kuddus Sheikh[1], Dominik Kowal[1], Muhammad Haris Mahyuddin[2], Roberto Cala'[3,4], Etiennette Auffray[4], Marcin Eugeniusz Witkowski[5], Michal Makowski[5], Winicjusz Drozdowski[5], Hong Wang[6], Christophe Dujardin[7], Daniele Cortecchia[8,*] Muhammad Danang Birowosuto[1,*]

[1] Łukasiewicz Research Network-PORT Polish Center for Technology Development,
Stabłowicka 147, Wrocław, 54-066, Poland;

[2] Faculty of Mathematics and Natural Sciences, Institut Teknologi Bandung, Jl. Ganesha 10,
Bandung, 40132, Indonesia;

[3] Dipartimento di Fisica, Università di Milano-Bicocca, Milan, 20126, Italy;

[4] CERN, Esplanade des Particules 1, 1211 Meyrin, Switzerland;

[5] Institute of Physics, Faculty of Physics, Astronomy, and Informatics, Nicolaus Copernicus
University in Toruń, ul. Grudziądzka 5, 87-100 Toruń, Poland;

[6] School of Electrical and Electronic Engineering, Nanyang Technological University, Singapore
639798, Singapore;

[7] Institut Lumière Matière, UMR5306, Université Claude Bernard Lyon1 and CNRS Lyon,
France;

[8] Dipartimento di Chimica Industriale "Toso Montanari", Università di Bologna, 40136 Bologna,
Italy.

* Corresponding author:

Email addresses: daniele.cortecchia2@unibo.it (Daniele Cortecchia),
muhammad.birowosuto@port.lukasiewicz.gov.pl (Muhammad Danang Birowosuto)

ABSTRACT

Quantum-well (QW) hybrid organic-inorganic perovskite (HOIP) crystals, e.g. A_2PbX_4 (A = BA, PEA, X = Br, I), demonstrated significant potentials as scintillating materials for wide energy radiation detection compared to their individual three-dimensional (3D) counterparts, e. g. $BPbX_3$ (B = MA). Inserting 3D into QW structures resulting new structures namely $A_2BPb_2X_7$ perovskite crystals and they may have promising optical and scintillation properties towards higher mass density and fast timing scintillators. In this article, we investigate the crystal structure, optical and scintillation properties of iodide-based QW HOIP crystals, A_2PbI_4 and $A_2MAPb_2I_7$. A_2PbI_4 crystals exhibit green and red emission with fastest PL decay time < 1 ns, while $A_2MAPb_2I_7$ crystals exhibit high mass density of > 3.0 g/cm^3, and tunable smaller band gaps < 2.1 eV resulting from quantum and dielectric confinement. We observe that A_2PbI_4 and $PEA_2MAPb_2I_7$ show emission under X- and γ-ray excitations. We further observe that some QW HOIP iodide scintillators exhibit shorter radiation absorption lengths (~3 cm at 511 keV) and faster scintillation decay time components (~0.5 ns) compared to those of QW HOIP bromide scintillators. Finally, we investigate the light yields of iodide-based QW HOIP crystals at 10 K (~10 photons/keV), while at room temperature they still show pulse height spectra with light yields between 1 and 2 photons/keV, which is still >5 times lower than those for bromides. The lower light yields can be the drawbacks of iodide-based QW HOIP scintillators, but the promising high mass density and decay time results of our study can provide the right pathway for further improvements towards fast-timing applications.

KEYWORDS

Quantum-well perovskites, absorption length, luminescence, light yields, scintillators.

INTRODUCTION

Hybrid organic-inorganic perovskite (HOIP) crystals have attracted significant attention due to their remarkable properties, including long carrier diffusion length, low defect density, possibly high absorption coefficient, medium exciton binding energy, tunable bandgap.[1,2,3,4,5,6,7] Such properties make them promising materials for next-generation optoelectronic applications.[8,9,10,11,12,13] In addition, the presence of the heavy lead (Pb) element is favorable to the absorption of high-energy X-rays and γ-rays. Despite their widespread applications and below-oven-furnace temperature processability, commercialization of these devices is hindered by their poor environmental stability. Quantum-well (QW) HOIP crystals, A_2PbX_4 [14], have shown remarkable environmental and thermal stability compared to their three-dimensional (3D) counterparts, $BPbX_3$ (B = methylammonium (MA)), while preserving significant optical and scintillation properties toward targeted applications.[14,15,16,17,18] These materials consist of inorganic perovskite slabs intercalated with bulky organic cations that act as spacers between these layers, adopting the crystal structure of the Ruddlesden-Popper (RP) type. In particular, QW HOIP crystals, as direct band gap materials, have demonstrated high potentialities as scintillating materials for fast timing applications in security, medical diagnosis, industrial sectors, high-energy physics, and materials science.[19,20,21,22] They exhibit high light yields > 10 photons/keV, short scintillation decay times < 15 ns leading to good coincidence time resolutions (CTR) < 150 ps.[21,23,10,8] However, the absorption length of typical QW HOIP are > 2 times longer than the commercial CsI:Tl scintillators[24] making the crystals less attractive for high energy excitation applications, such as time of flight positron emission tomography which is operating at 511 keV (TOF-PET).[20] In addition, so far QW HOIP scintillators have been reached with bromide of (Br) variants with 3 eV bandgaps (e.g. phenethylammonium lead bromide $(PEA)_2PbBr_4$ and n-butylammonium lead bromide $(BA)_2PbBr_4$), still possess scintillation light yields about half from 66 photons/keV of commercial CsI:Tl scintillator.[20] To improve the yields, one can look to lower bandgap materials such as 3D HOIP or iodide (I) crystals with 2 eV bandgaps. They may provide higher light yields although so far the light yields were recorded at low temperature.[19] To achieve better absorption lengths and light yields, one should get higher density materials and smaller bandgaps, respectively.[20] For the faster decay time, one has to search iodide (I^-) crystals of QW HOIP, as most crystals exhibit decay times of < 2 ns but lower light yield.[16] This requires a modulation of the crystals properties between those of QW and 3D

HOIP structures, which can be synthetically achieved exploiting the versatility of the Ruddlesden-Popper compositions $A_2B_{n-1}Pb_nI_{3n+1}$ (where n is an integer). Such materials allow the full control of the optoelectronic properties either by compositional engineering or by structural modulation exploiting different levels of quantum and dielectric confinement in materials with different dimensionalities (n). Among the numerous reported perovskite-based optoelectronic devices, including solar cells,[7,25,26,27] field-effect transistors (FETs),[28] light-emitting diodes (LEDs),[29,30] and photodetectors[31], many are based on powders and thin films. Particularly, $PEA_2MA_{n-1}Pb_nI_{3n+1}$ compounds which exhibit multiple quantum-well structures are extensively investigated for application light emitting diodes (LEDs) due to their excellent photoluminescence (PL) properties. However, there have been hitherto no reports available on the $A_2B_{n-1}Pb_nI_{3n+1}$ materials utilized as scintillators.

In this article, we synthesize four different Ruddlesden-Popper iodide-based QW HOIP crystals with n = 1, 2 as n is the number of 3D structures sandwiched between QW layers. We investigate the crystal structure, optical and scintillation properties of $(PEA)_2PbI_4$, $(BA)_2PbI_4$ and the corresponding n = 2 RP phases $(PEA)_2MAPb_2I_7$ and $(BA)_2MAPb_2I_7$. $(PEA)_2PbI_4$ was previously discussed by our group in a short report by comparing different methods in crystal fabrications for light yield optimization.[32] Here we present the global trend in optical and scintillation properties with other unreported properties from other three iodide structures. We show that $(BA)_2PbI_4$ and $(PEA)_2PbI_4$ crystals exhibit green and red emission with the fastest PL decay time. We further find that n = 2 layered perovskite iodide scintillators exhibit a mass density of > 3.0 g/cm^3, and tunable rather small band gaps < 2.1 eV resulting from quantum and dielectric confinement due to the dimensional reduction of the perovskite spacer layers compared to 3D structures. Among these, we observe that only $(PEA)_2MAPb_2I_7$ shows emission under X- and γ-ray excitations. From all these iodide crystals, we find light yields at room temperature (RT) (1-2 photons/keV) considerably lower than those of $(BA)_2PbBr_4$ and $(PEA)_2PbBr_4$ (10-40 photons/keV), while at 10 K, the light yields is comparable (~10 photons/keV).[16] Thus, applications at low temperature are envisaged when shorter radiation absorption length (~3 cm at 511 keV) and faster decay time component (~0.5 ns) are foreseen. Such results may provide a new pathway for further improvements of these materials towards fast-timing applications.

- **MATERIALS AND METHODS**

Materials: Methylammonium chloride (MACl), 50% aqueous (H_3PO_2), lead oxide (PbO, 99.999%), phenethylamine (99%), n-butylamine (>99%), 57% stabilized hydroiodic acid (HI), lead iodide (PbI_2, 98%), dimethyl sulfoxide (DMSO, anhydrous), n-butylammonium bromide ((BA)Br, ≥ 98%)), phenethylammonium bromide ((PEA)Br, ≥ 98%), and lead bromide ($PbBr_2$, ≥ 98%) were purchased from Sigma-Aldrich.

Synthesis of QW HOIP crystals: The QW A_2PbI_4 crystals were synthesized using a method previously reported by Kowal et. al.[32] The QW A_2PbBr_4 crystals were synthesized using a modified version of the previously reported method.[14,33] A 3 M precursor solution was prepared by dissolving (BA)Br or (PEA)Br and $PbBr_2$ in in stoichiometric amounts in DMSO under stirring at 100 °C for 2h. The crystal precipitate was then washed with hexane and dried under vacuum for future characterization. For $A_2MAPb_2I_7$ crystals, PbO (223.2 mg) and MACl (200 mg for PEA and 33.8 mg for BA) powders were dissolved in aqueous HI solution (2 mL for PEA and 1 mL for BA) with the addition of 50% aqueous H_3PO_2 (0.17 mL). Separately, 88.2 µL of PEA and 69.4 µL of BA were neutralized with 0.5 ml of HI 57% w/w, respectively causing the precipitation of a white solid that re-dissolved upon heating. The PEA or BA solution was added to the PbO/MACl solution, and the mixture heated at 150 °C under magnetic stirring on a hotplate. The solution was transferred in an oven where it was kept for 24 h and during this time the temperature from 100 °C to 20°C, allowing the growth of red crystals for PEA- and dark red crystals for BA-based $A_2MAPb_2I_7$, respectively. These were collected by filtration and dried at 100 °C under vacuum. The obtained perovskite crystals were stored in the glovebox under inert atmosphere.

X-ray diffraction: Bruker D8 Advance AXS diffractometer was used for measuring powder X-ray diffraction (XRD) spectra of the synthesized compounds[32]. The device used Cu Kα radiation with the 1.5418Å wavelength. Measurements were conducted at RT, under Bragg-Brentano geometry, 5 s/step scanning velocity and 0.02° step size. FullProf Suite software was then used to analyze the acquired data.

PL, TRPL, and absorption: For PL measurements the samples were excited with the use of picosecond laser diode with repetition rate 30 MHz and 375 nm o 532 nm wavelength (Master Oscillator Fibre Amplifier, Picoquant GmbH, Berlin, Germany, pulse duration 50 ps and 10 mW average power. Microscopic objective with numerical aperture (NA) 0.4 and magnification 20x (Nikon Corporation, Tokyo, Japan) was used for excitation focusing and signal collection. The filtered PL signal was acquired by high sensitivity visible light spectrometer (Ocean Optics, Florida, USA). For TRPL measurements, the repetition rate was reduced to 10 MHz and the PL signal, selected by bandpass filter 532 ± 25 nm, was coupled to a single-photon avalanche photodiode (APD). The timing response was analyzed by time-correlated single-photon counting electronics(HydraHarp 400, PicoQuant, Germany). Tungsten Halogen light source (Ocean Optics LS-1) and same visible light spectrometer as for the PL experiments were used to measure the absorption of the samples in the transmission mode. All measurements were conducted at RT.

RL, TL, and afterglow curves: The X-ray excitation was provided by an Inel XRG3500 X-ray generator Cu-anode tube(45 kV / 10 mA). For recording the optical signal we used Acton Research Corporation SpectraPro-500i monochromator, a Hamamatsu R928 photomultiplier tube (PMT), and an APD Cryogenic Inc. closed-cycle helium cooler. The crystals were exposed to X-ray radiation for 10 min and the afterglow curve was recorded at temperature of 10 K. Then, TL glow curves were measured from 10K to 350 K by increasing the temperature, with 0.14 K/s heating rate. Finally, RL signal was measured from 350K to 10 K by cooling down the sample back. Measurement started from the highest temperature as to avoid thermal release of charge carriers which could possibly contribute to the emission yield.

Pulse height and scintillation decay measurements: For source of the γ-rays, 137Cs (662 keV, 210 kBq) radioisotope was used and the converted photons were detected by PMT (Hamamatsu R878) with 1.25 kV applied voltage. The output was integrated with charge sensitive pre-amplifier (Canberra 2005) and then it fed a spectroscopic amplifier (Canberra 2022) with a shaping time of 2 μs and a TUKAN-8K-USB multichannel analyzer. In the pulse height spectrum the position of the photopeak was compared with the position of the mean value of the single electron response to obtain the photoelectron yield. The actual light yield for the radiation conversion in photons per MeV was obtained by taking into consideration the spectral matching of the sample luminescence to the PMT characteristics. Scintillation decay measurements were performed by the delayed coincidence single photon counting method.[16] A ^{137}Cs radioactive source, two Hamamatsu photomultiplier tubes (R1104 and R928 for “starts” and “stops”, respectively), a Canberra 2145 time to-amplitude converter, and a TUKAN-8K-USB multichannel analyzer were used.

DFT calculations: The Kohn-Sham formulation[34] as implemented in the Vienna Ab initio Simulation Package (VASP)[35] was used for the DFT calculations. The Projector Augmented Wave (PAW) method[36] was used to describe the interaction between ion cores and electrons. The details of the simulation set up and the parameters used were the same as reported in [32].

RESULTS AND DISCUSSION

Photographs of $(PEA)_2PbI_4$ and $(PEA)_2MAPb_2I_7$ crystals, excited by 375 nm laser beam are displayed in Figs. 1(a), (b) and their crystal structures are shown in Figs. 1 (c), (d), respectively. The triclinic $(PEA)_2PbI_4$ and orthorhombic $(BA)_2PbI_4$ belongs to the class of two-dimensional (2D) A_2PbX_4 (A = PEA, BA; X = Br, I) HOIP and consist of the stack of ⟨100⟩-oriented perovskite inorganic layers, forming a 2D Pb-X octahedra network in alternation with the organic sheets of PEA and BA cations as displayed in Figs. 1(c), (e). Schematically, 2D HOIP crystals exhibit a layered structure[37,16], like QW, with inorganic $[PbI_6]^{4-}$-octahedra sheets separated by another layer of organic ammonium cations. The ball and stick structures of the n=2 compounds $A_2MAPb_2I_7$ (A = PEA, BA) are shown in Fig. 1(d), (f), where all diagrams include the $\{PbI_6\}$ octahedral units. Moreover, PEA^+ and MA^+ organic cations were so disordered that the benzene ring and MA^+ cation could be hardly distinguished. Significant disorder exists in the interlayer cations of $(BA)_2MAPb_2I_7$ crystal, particularly for the CH_3CH_2- tail of butylammonium (the ligand head, $NH_3CH_2CH_2$- is relatively stable), causing the atoms to move and destabilize the refinement.[37]

Powder X-Ray Diffraction (XRD) patterns of ground perovskite crystals are shown in Fig. 2(a). The prominent low-angle diffraction peaks of A_2PbX_4 are indicative of their (002 preferential orientation, while the preferential orientation of $A_2MAPb_2I_7$ (A = PEA, BA) occurs in the lattice planes of (2-14), (111), respectively, as displayed in Fig. 2(a). The XRD patterns of the four crystals were analyzed with the Rietveld refinement method using the FullProf software. [38,39,40,41] and the results are shown in Table I and diffractograms of $(PEA)_2PbI_4$, $(PEA)_2MAPb_2I_7$, $(BA)_2PbI_4$, and $(BA)_2MAPb_2I_7$ including photographs of corresponding crystals in Fig. S1. The triclinic phase was found with $P\overline{1}$ space group for $(PEA)_2PbI_4$ and *P1* for $(PEA)_2MAPb_2I_7$. The $(PEA)_2MAPb_2I_7$ single crystals mostly represented a triclinic lattice structure at RT.[40,41] On the other hand, orthorhombic phase can be found with primitive centrosymmetric *Pbca* space group for $(BA)_2PbI_4$[42] and *Cc2m* space group for $(BA)_2MAPb_2I_7$.[42,37,43] Due to the larger size of iodide than bromide, $(PEA)_2PbI_4$ crystal shows 209.60 $Å^3$ and $(BA)_2PbI_4$ crystal shows 219.14 $Å^3$ larger volume compared to their corresponding bromide crystal, respectively. The volume for $(PEA)_2MAPb_2I_7$ crystal is 378.95 $Å^3$ larger than $(BA)_2MAPb_2I_7$ crystal which is due to the larger size of PEA compared to BA cation.

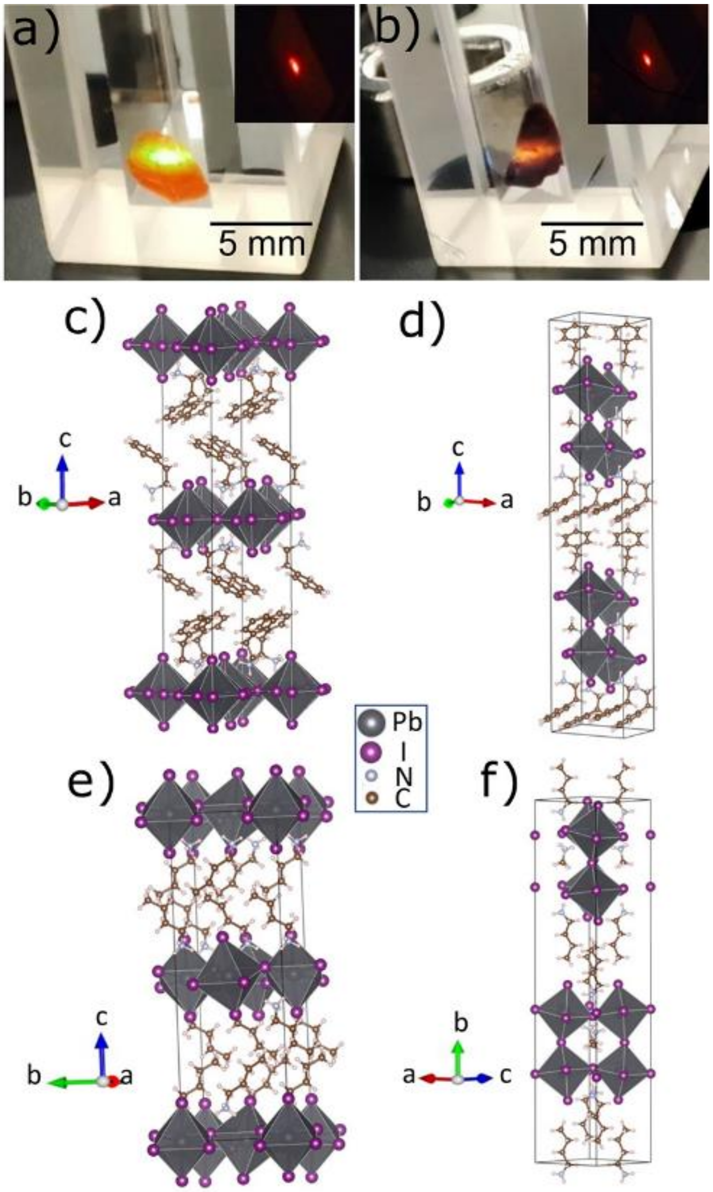

Fig. 1. Photographs of (a) $(PEA)_2PbI_4$, and (b) $(PEA)_2MAPb_2I_7$ crystals under 375 nm laser excitation. The insets correspond to red emission at 532 nm excitation wavelength. Schematic crystal structures of (c) $(PEA)_2PbI_4$, (d) $(PEA)_2MAPb_2I_7$, (e) $(BA)_2PbI_4$, and (f) $(BA)_2MAPb_2I_7$ perovskite.

Table I Summary of the crystal data, structure refinements, and bandgaps calculated absorption spectra (E_g^{abs}) and other parameters for $(PEA)_2PbI_4$, $(PEA)_2MAPb_2I_7$, $(BA)_2PbI_4$, $(BA)_2MAPb_2I_7$ crystals at 298 K. The term absorption length is denoted as ℓ.

	$(PEA)_2PbI_4$	$(PEA)_2MAPb_2I_7$	$(BA)_2PbI_4$	$(BA)_2MAPb_2I_7$
Empirical formula	$C_{16}H_{24}N_2PbI_4$	$C_{17}H_{30}N_3Pb_2I_7$	$C_8H_{24}N_2PbI_4$	$C_9H_{30}N_3Pb_2I_7$
Formula weight	959.17	1579.12	862.90	1483.04
Crystal system	Triclinic	Triclinic	Orthorhombic	Orthorhombic
Space group	$P\bar{1}$	$P1$	$Pbca$	$Cc2m$
a (Å)	8.5835	8.8015	8.2950	8.9785
b (Å)	8.6833	8.8130	9.2310	39.4140
c (Å)	33.2053	45.7276	27.6290	8.8524
α (˚)	85.1511	97.0364	90.0000	90.0000
β (˚)	85.1281	93.9577	90.0000	90.0000
γ (˚)	90.3921	90.1823	90.0000	90.0000
V (Å^3)	2456.8819	3511.6297	2115.5841	3132.6751
Z	4	4	4	4
ρ (g/cm^3)	2.59	3.00	2.73	3.14
E_g^{abs} (eV)	2.35	2.05	2.41	1.97
E_g^{cal} (eV)	2.13	2.10	2.24	1.80
ℓ @50 keV (cm)	0.050	0.039	0.042	0.035
ℓ @511 keV (cm)	3.93	3.22	3.59	3.02
PL peak (eV)	2.35	2.15	2.39	2.13

Fig. 2(b) presents the calculated absorption lengths [44] for photon energies up to 511 keV. and the insets correspond to the magnified X-ray spectral region at 50 keV and γ-ray spectral region at 511 keV. The mass density (ρ) of $(PEA)_2PbI_4$, $(PEA)_2MAPb_2I_7$, $(BA)_2PbI_4$, and $(BA)_2MAPb_2I_7$ crystals are calculated of 2.59 g cm^{-3}, 3.00 g cm^{-3}, 2.73 g cm^{-3}, and 3.14 g cm^{-3}, respectively.[45,32] Iodide (I^-) HOIP crystals have higher ρ than $(PEA)_2PbBr_4$ (2.28 g cm^{-3}) or $(BA)_2PbBr_4$ (2.36 g cm^{-3}) crystals, respectively.[46] Due to the larger atomic size of iodide compare to bromide shows high mass density. In our works, ρ values of $(PEA)_2MAPb_2I_7$, and $(BA)_2MAPb_2I_7$ crystals are similar in comparison to the reported 3.00 g cm^{-3},[40] and 3.16 g cm^{-3},[37] respectively. As a result, all absorption lengths (ℓ) at 50 keV of those iodide crystals are at least 50% shorter than those of bromides (ℓ of $(BA)_2PbBr_4$ is 0.099 cm).[46] However, those ℓ become at least 5% shorter at 511 keV.[46] The $(BA)_2MAPb_2I_7$ has the shortest absorption length of all the studied crystals as can be seen from the Fig. 2(b). At 50 keV which is widely used in X-ray imaging, ℓ of $(PEA)_2PbI_4$ is 0.050 cm, 16% longer than ℓ of $(BA)_2PbI_4$ of 0.042 cm, and for $(PEA)_2MAPb_2I_7$ is 0.039 cm, just 11% longer than ℓ of $(BA)_2MAPb_2I_7$ of 0.035 cm. The effect of the PEA cation on the density leads to a 20% longer ℓ for A_2PbI_4 and 6% shorter ℓ for $A_2MAPb_2I_7$ compared to their BA cation crystals at 511 keV, respectively and the results are summarized in Table 1. For TOF PET, longer ℓ of $(PEA)_2PbI_4$ among the four crystals are still 44% longer at 50 keV and 50% longer at 511 keV than that of commercial scintillator, CsI:Tl.[20,24]

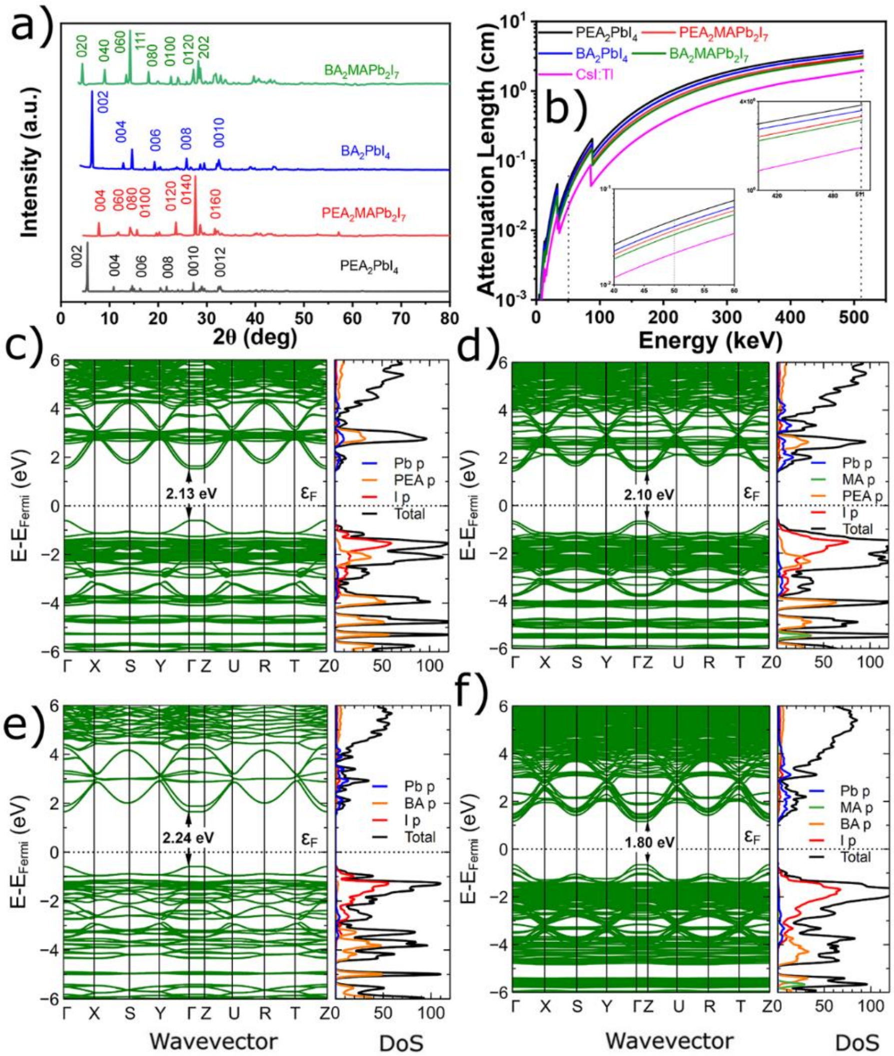

Fig. 2. (a) X-ray diffraction pattern of the crystals. (b) Absorption lengths ℓ calculated for X-ray and γ-ray spectral region. Inset corresponds to the magnified X-ray spectral region at 50 keV and γ-ray spectral region at 511 keV. The band structure, total (black) and projected (color) DOS of (c) $(PEA)_2PbI_4$, (d) $(PEA)_2MAPb_2I_7$, (e) $(BA)_2PbI_4$ and (f) $(BA)_2MAPb_2I_7$ crystals. The Pb p, PEA p, BA p, MA p, and I p are represented by blue, orange, pink, green, and red lines respectively

The ab-initio components for the scintillation efficiencies can be studied through their band structures. Therefore, we employ the density functional theory (DFT) method to calculate the density of states (DOS) and determine the optical bandgap (E_g). The band structures with their total (black) and projected (color) DOS of the studied perovskite crystals are shown in Fig. 2(c), (d), (e), and (f), respectively. From the calculations., the band structures of all iodide-based QW HOIPS show direct-band-gap characteristics.

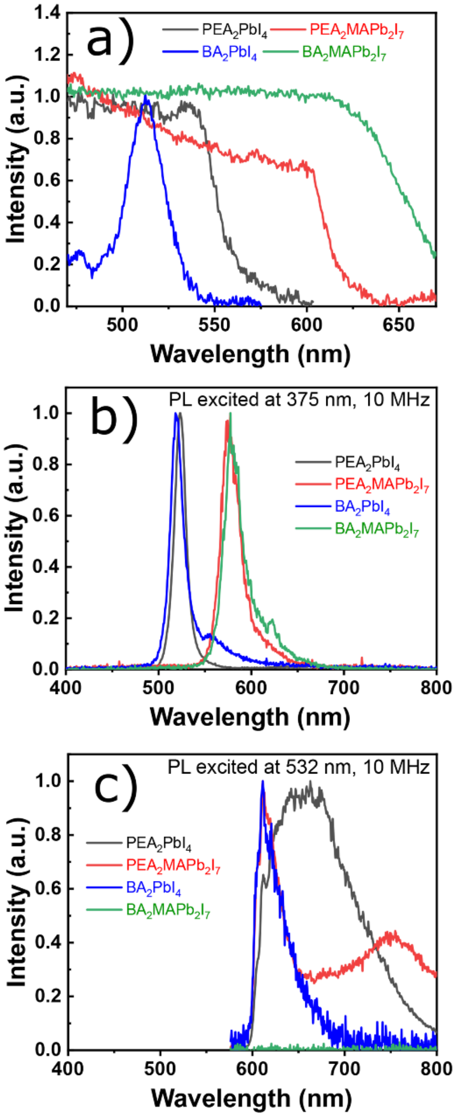

Fig. 3. (a) Absorption; PL spectra of $(PEA)_2PbI_4$, $(PEA)_2MAPb_2I_7$, $(BA)_2PbI_4$, and $(BA)_2MAPb_2I_7$ perovskites recorded at room temperature (RT) and excited at (b) 375 nm, and (c) 532 nm, respectively.

We obtained the calculated bandgaps (E_g^{cal}) of 2.13 eV, 2.10 eV, 2.24 eV, and 1.80 for $(PEA)_2PbI_4$, $(PEA)_2MAPb_2I_7$, $(BA)_2PbI_4$, and $(BA)_2MAPb_2I_7$, respectively, the former of $(PEA)_2PbI_4$ shows similar reported values of (2.13),[40,32] the $(BA)_2PbI_4$ shows similar reported values of 2.28 eV,[47] and the later of $(PEA)_2MAPb_2I_7$ shows smaller than reported values of 2.31 eV.[48] To compare E_g^{cal}, we performed absorption measurements while their spectra and their corresponding bandgap fitting curves are shown in Fig. S2. On one hand, we obtained small differences of 0.22 and 0.31 eV between E_g^{cal} and calculated Elliot fit bandgaps (E_g^{fit}) of 2.35, and 2.41 eV for $(PEA)_2PbI_4$, and $(BA)_2PbI_4$, respectively. On the other hand, we obtained 2.05 eV and 1.97 eV calculated from Elliot fit for $(PEA)_2MAPb_2I_7$ and $(BA)_2MAPb_2I_7$ crystals, respectively. The band gap of 2.05 eV for $(PEA)_2MAPb_2I_7$ crystal is larger compared to reported one of 1.86 eV[40] and the band gap of 1.97 eV for crystal is coherent with reported value of 1.99 eV.[27]

Optical and PL measurements were performed on bulk crystals of $(PEA)_2PbI_4$, $(PEA)_2MAPb_2I_7$, $(BA)_2PbI_4$, and $(BA)_2MAPb_2I_7$ (Fig. 3). Absorption spectra recorded at RT are shown in Fig. 3 (a) and Elliot fit of these absorption spectrum were performed by Elliot formalism[49] (Fig. S2). In addition, absorption and PL spectra excited at 375 nm with a logarithmic scale of y-axis recorded at RT, decay curve and photographs of corresponding $(PEA)_2PbBr_4$, $(BA)_2PbBr_4$ crystals are shown in Fig. S3. PL spectra recorded at RT in Figs. 3(b), (c) exhibit two different emission origin depending on the excitation wavelength. On one hand, exciting the samples with 375 nm wavelength produces an emission band at 532 nm (green) for $(PEA)_2PbI_4$, $(BA)_2PbI_4$ and 577 nm (yellow) for $(PEA)_2MAPb_2I_7$, and $(BA)_2MAPb_2I_7$ crystals that is much more intense than the band at 620 nm (red). On the other hand, when using the longer wavelength excitation of 532 nm only one red emission band is observed at 620 nm (red) for $(BA)_2PbI_4$ and a broad band at 660 nm (red) for $(PEA)_2PbI_4$, and red emission at 620 nm at its band gap energy (2.0 eV) with an appreciable PL emission broad band at 748 nm which could originate from the edges of the exfoliated layers of perovskite crystal, as reported by Blancon et al.[50] for $(PEA)_2MAPb_2I_7$ crystals. The broadband of PEA_2PbI_4 crystal at 660 nm is possibly due to the radiative path of electron capture at a positive iodide vacancy with subsequent hole capture.[51] There is no emission band observed for $(BA)_2MAPb_2I_7$ crystal at 532 nm excitation wavelength. The green emission band has full-width-at-half-maximum (FWHM) equal to 19 nm for $(PEA)_2PbI_4$, and $(BA)_2PbI_4$ and 22 nm for $(PEA)_2MAPb_2I_7$, and $(BA)_2MAPb_2I_7$ while the red band is broad (110 nm) for $(PEA)_2PbI_4$ and narrow (32 nm) for $(BA)_2PbI_4$ and $(PEA)_2MAPb_2I_7$. The PL characteristics were observed for $(PEA)_2PbI_4$ and $(PEA)_2MAPb_2I_7$ crystals that were synthesized using PbI_2 precursor and additionally treated with PEAI.[38] The origin of the green emission band is the characteristic excitonic emission from inorganic PbI_2 layers while the red emission is associated with the the in-plane iodide vacancy causing surface states.[38]

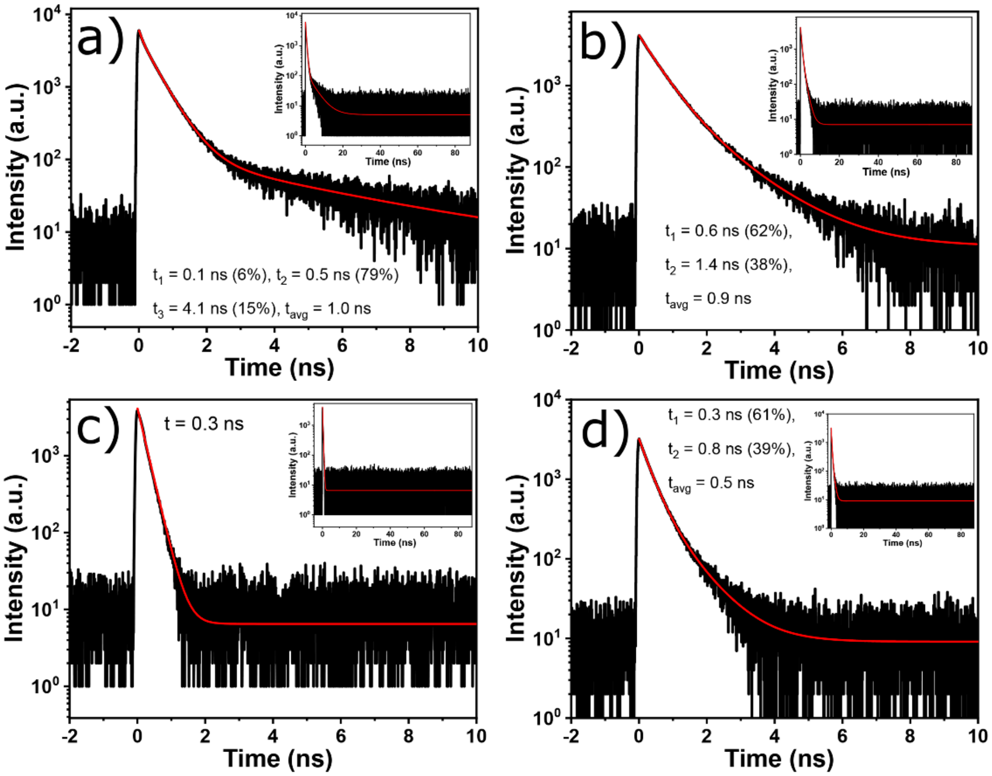

Fig. 4. TRPL decay curve excited at 375 nm monitoring 532 nm emission of (a) $(PEA)_2PbI_4$, and (c) $(BA)_2PbI_4$; 577 nm emission of (b) $(PEA)_2MAPb_2I_7$, and (d) $(BA)_2MAPb_2I_7$ crystals, respectively. The fits are shown with red lines while the insets correspond to longer time scales.

We probed the spectral origin of the emitting states observed using PL excitation and time-resolved PL (TRPL) spectroscopy. The TRPL decay curves of perovskite crystals were fitted by exponential decay functions which is shown in Figs. 4a-d. Most decay times in iodide QW HOIP crystals are faster than those in bromide QW HOIP crystals, see Fig. S3, as they can affect the scintillation decay times. Such <1ns fast decay components of iodide QW HOIP crystals are also observed in previous observations of QW HOIPs.[16,22,32] To do the analysis, we also presented RT decay curves excited at 532 nm monitoring 620 nm emission in Fig. S4. The decay components for the 532 nm emission band of the $(PEA)_2PbI_4$ crystal were found as 0.1, 0.5 and 4.1 ns and they are associated with free-exciton emission. The average lifetime value τ_{avg}^{PL} of 1.0 ns is similar to those reported in ref.[38] The decay components at 620 nm were 3.6 ns and 37.7 ns and τ_{avg}^{PL} of 36.6 ns which is 36.6 times slower than τ_{avg}^{PL} at 532 nm, see Fig. S4. The fastest decay time of 0.3 ns was observed at 532 nm and 0.4 ns at 620 nm for $(BA)_2PbI_4$ crystal which is about 4 times and 99 times faster than τ_{avg}^{PL} at 532 and 620 nm of $(PEA)_2PbI_4$ crystal, respectively. On the other hand, the decay components for $(PEA)_2MAPb_2I_7$ crystal of 0.6 and 1.4 ns correspond to the exciton emission as the decay curve was measured for the 577 nm emission band and τ_{avg}^{PL} of 0.9 ns, while the decay components at 620 nm emission peak position were 0.4 ns and 7.2 ns and τ_{avg}^{PL} of 4.5 ns which is 5 times slower than τ_{avg}^{PL} at 577 nm emission. The fast decay components for $(BA)_2MAPb_2I_7$ crystal of 0.3 and 0.8 ns correspond to the exciton emission as the decay curve was measured for 577 nm emission band only and τ_{avg}^{PL} of 0.5 ns was observed. Although for $(PEA)_2PbI_4$ and $(PEA)_2MAPb_2I_7$ crystals, the decay times at 577 nm emission are fast, the presence of the emission for respective emission bands at 660 and 748 nm in Fig. 3c can make the scintillation decay curves slower as the TRPL monitoring 620 nm emission exhibit slower decay components >8 ns, see Fig. S4. As expected from the absence of the long wavelength band in BA_2PbI_4 crystal in Fig. 3c, the decay time at 620 nm also yields similar value as that at 532 nm, see Figs. 4c and S4c for comparison.

The radioluminescence (RL) spectra at RT in Fig. 5(a) are dominated by the red broadband emission, which resembles the red emission band in PL spectra excited with 532 nm wavelength in Fig. 3(a) for $(PEA)_2PbI_4$ and $(PEA)_2MAPb_2I_7$ crystals. The fact that the red surface defect emission (630-665 nm) dominates against the green exciton emission (520-545 nm) for $(PEA)_2PbI_4$ and $(PEA)_2MAPb_2I_7$ crystals excited by X-ray in temperature-dependent RL spectra is due to self-absorption.[16,52] On the other hand, the green surface defect emission (660 nm) strongly dominated compared to red emission (700 nm) for $(BA)_2PbI_4$ crystal and there was no emission excited by X-ray for $(BA)_2MAPb_2I_7$ crystal. However, the (PEA)2PbI4 crystal shows higher self-absorption compared to $(BA)_2PbI_4$ crystal and over all the self-absorption of $(PEA)_2MAPb_2I_7$ crystal was much more stronger among all the crystals, due to presence of $MAPbI_3$ impurities.[48] Afterglow decay recorded after 10 minutes of X-ray irradiation at 10 K curve of $(PEA)_2PbI_4$, $(PEA)_2MAPb_2I_7$, $(BA)_2PbI_4$, and $(BA)_2MAPb_2I_7$ crystals, respectively are shown in Fig. 5(b). The details of afterglow decay components parameters are reported in Table S1. The afterglow decay components for $(PEA)_2PbI_4$ were 4.9 s (10%), 33.1 s (32%) and 364.3 s

(58%) and the average value of afterglow times $\tau_{avg}^{afterglow}$ is 224.1 s, while for $(BA)_2PbI_4$ crystal they were 0.2 s (2%), 15.7 s (26%) and 166.5 s (72%) and $\tau_{avg}^{afterglow}$ of 87.4 s, respectively. On the other hand, the afterglow decay components for $(PEA)_2MAPb_2I_7$ crystal were 9.6 s(1%), 121.6 s (4%), 4560.1 s (95%), and $\tau_{avg}^{afterglow}$ of 4336.5 s, while for $(BA)_2MAPb_2I_7$ crystal were 6.5 s (35%), 66.5 s (65%), and $\tau_{avg}^{afterglow}$ of 45.4 s. The fastest afterglow was observed for $(BA)_2PbI_4$ which is 5 times faster than $(PEA)_2PbI_4$. Afterglow for A_2PbI_4 crystals were faster than that observed in $A_2BPb_2I_7$ crystals due to low trap density. The presence of traps is directly related with the chain length of organic cation.[53] We examine the presence of trap states in the investigated scintillators by performing thermoluminescence (TL) measurements. TL is the phenomenon of afterglow with temperature of a previously exposed materials by high energy radiation. Originally the thermally activated afterglow is due to the phonon-assisted release of trapped charge carriers with temperature, leading to radiative recombination.[16,33]

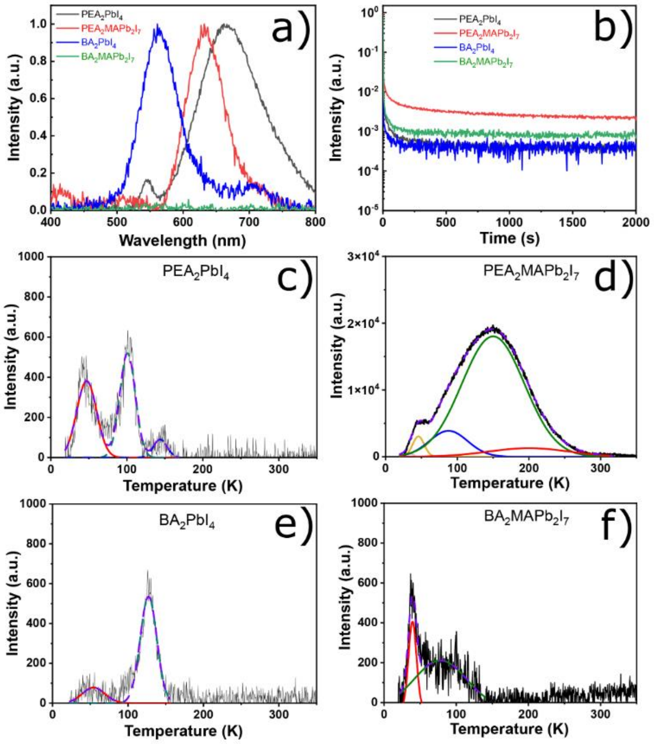

Fig. 5. (a) RL spectra at RT; (b) Afterglow decay curves at 10 K of $(PEA)_2PbI_4$, $(PEA)_2MAPb_2I_7$, $(BA)_2PbI_4$, and $(BA)_2MAPb_2I_7$ crystals, respectively. Afterglow parts were recorded after 10 minutes of X-ray irradiation. TL spectra and corresponding fits of (c) $(PEA)_2PbI_4$, (d) $(PEA)_2MAPb_2I_7$, (e) $(BA)_2PbI_4$, and (f) $(BA)_2MAPb_2I_7$ crystals, respectively.

TL spectra and corresponding fits are shown in Figs. 5(c-f) and TL parameters in Table S2 for $(PEA)_2PbI_4$, $(PEA)_2MAPb_2I_7$, $(BA)_2PbI_4$, and $(BA)_2MAPb_2I_7$, respectively. All samples show several glow peaks as the temperature of the sample is raised, indicating the presence of traps in the crystals. Unfortunately, those traps are mostly deeper and they have more trapped charge carries than those in $(PEA)_2PbBr_4$ and $(BA)_2PbBr_4$.[46] The glow peaks for $(PEA)_2PbI_4$ crystal were observed at temperature 47 K, 101 K, and 144 K with trap density of 1.2×10^4, 1.3×10^4, and 2.1×10^3, respectively, as shown in Fig. 5(c). Significant and several glow peaks with less noisy result for $(PEA)_2MAPb_2I_7$ crystal were observed due to the high intensity and more traps as summarized in the Table S2 including deep trap over a long temperature range (up to 200 K) as shown in Fig. 5(d). On the other hand, negligible glow peaks were observed at temperature 54 K, and 127 K with trap density of 2.9×10^3, and 1.5×10^4, respectively, for $(PEA)_2PbI_4$ crystal as shown in Fig. 5(e) and 39 K, and 78 K with trap density of 1.1×10^4, and 5.5×10^3, respectively, as shown in Fig. 5(f). $A_2MAPb_2I_7$ HOIP crystals specially for $(PEA)_2MAPb_2I_7$ crystal shows more traps due to presence of $MAPbI_3$ impurities[48] which has strong traps.[54] In addition, $(PEA)_2MAPb_2I_7$ crystal has traps over a wide range of temperature from 30 K to 250 K.

Light yield is an important property of a scintillator, *i.e.* the efficiency of the scintillator to convert the energy of absorbed X- and γ-rays into visible photons.[20] RL measurements were used to determine the comparative values of light yields for perovskite scintillators.[19,55] The γ-ray pulse height method gives quantitative values for the light yield and also provides information on the energy resolution of the scintillator. Note that the pulse height method is time resolved while the RL comparison is in the steady state mode. The light yield is the comparison of the photopeak signals in the pulse height spectra at certain energy of γ-ray radiation with the scintillator single electron response.[33] Fig. 6(a) present the results for pulse height spectra recorded under γ-ray excitation. The pulse height spectrum in Fig. 6(a) for $(PEA)_2PbI_4$, $(BA)_2PbI_4$, and $(PEA)_2MAPb_2I_7$ crystals exhibit structures of Compton scattering and photoelectric peak, however the obtained energy resolution value was above 32 % which is still far from beating the best energy resolution result for lithium-doped $(PEA)_2PbBr_4$ of 7.7% at 662 keV from the ^{137}Cs source of γ-ray excitation.[16] Fig. 6(b) shows the temperature-dependent normalized light yield under 45 keV X-ray excitation.

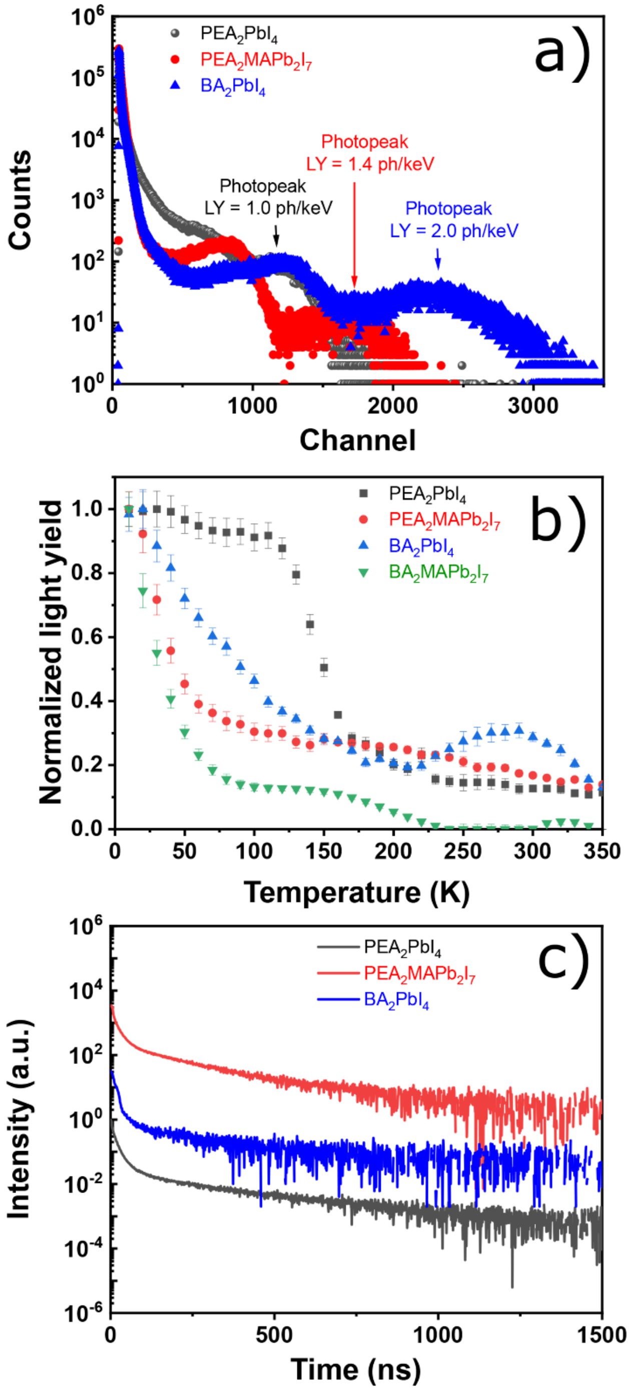

Fig. 6. (a) Integrated pulse height in the logarithmic scale. (b) Temperature-dependent light yield from 10 K to 350 K under 45 keV X-ray excitation of $(PEA)_2PbI_4$, $(PEA)_2MAPb_2I_7$, $(BA)_2PbI_4$, and $(BA)_2MAPb_2I_7$ crystals, respectively. (c) Scintillation decay curves of $(PEA)_2PbI_4$, $(PEA)_2MAPb_2I_7$, and $(BA)_2PbI_4$. For the γ-ray source a^{137}Cs emitting at 662 keV was used.

Based on the integration of the RL intensities at each temperature, the light yield was calculated. Under X-ray excitation, large amounts of charge carries are involved, leading to the large possibility of trapping.[16] As shown in Fig. S5, the temperature-dependent RL 2D maps of some HOIP crystals illustrate their different patterns. Due to the negative thermal quenching behaviors, bromide HOIP crystals have maximum light yields at temperatures close to RT,[16] while iodide HOIP crystals suffer from the regular thermal quenching, so their light yields at RT as not as high with those at low temperatures. At 10 K, all samples exhibit the maximum light yields, which then gradually decrease by temperature raising. By comparing the organic cation of A_2PbI_4 or $A_2MAPb_2I_7$ HOIP crystals with the same iodide, for instance, $(PEA)_2PbI_4$ and $(BA)_2PbI_4$ or $(PEA)_2MAPb_2I_7$ and $(BA)_2MAPb_2I_7$, it is evident that PEA cation ones have higher light yields. The light yield (LY), expressed in photons/MeV, is given by the relation:

$$LY \propto (S\times Q)/E_g \qquad (1)$$

where S denotes the electron-hole transport efficiency to the exciton recombination, Q signifies the luminescence quantum efficiency of the exciton. There are also losses during the transport of the light in the detector due to internal scattering and re-absorption, so the actual light yield of the scintillator might be less than expected, depending on the geometry of the scintillator.[20] The light yields of all QW HOIPS are summarized in Table S3. $(BA)_2PbI_4$ has the highest light yield of 2 photons/keV among all crystals while $(PEA)_2PbI_4$ has 1 photons/keV at RT. The light yield of $(BA)_2PbI_4$ has improved both at RT and 10 K compared to the reported[16] one as shown in Table S3 due to different fabrication method. Since $(BA)_2PbI_4$ has slightly larger E_g of 0.1 eV, we expect the light yield to be smaller, but it is appearing that $(BA)_2PbI_4$ has larger Q and/or S than $(PEA)_2PbI_4$. This can be seen in the trend between $(BA)_2PbBr_4$ and $(PEA)_2PbBr_4$.[52,33] For $(PEA)_2MAPb_2I_7$, the light yield is slightly improved than $(PEA)_2PbI_4$ since the bandgap is smaller (2.10 eV). The smallest bandgap for $(BA)_2MAPb_2I_7$ is 1.80 eV and shows very small light yield at RT (see also Fig. S5) because there is a strong quenching since the bandgap is too small.[56] The maximum light yield of $(PEA)_2PbBr_4$ crystal at RT was 10 photons/keV,[57,58] larger than the iodide based QW HOIP crystal scintillators. The light yield for $(PEA)_2MAPb_2I_7$ crystal is 1.4 photons/keV at RT, respectively which is still low compared to the $(BA)_2PbI_4$ HOIP scintillator of 2 photons/keV. On the other hand, $(PEA)_2MAPb_2I_7$ scintillator has a pulse height spectrum which is slightly higher than $(PEA)_2PbI_4$ scintillator. Since the light yields at RT were observed in three crystals, delay distribution and the coincidence timing resolution (CTR) measurement results for $(PEA)_2PbI_4$, $(BA)_2PbI_4$ and $(PEA)_2MAPb_2I_7$ crystals are shown in Ref.[32] and Fig. S6, respectively. We obtained CTR of 138 ± 5 ps, 149 ± 10 ps, 207 ± 14 ps for

$(PEA)_2PbI_4$, $(BA)_2PbI_4$ and $(PEA)_2MAPb_2I_7$ crystals, respectively, and all still have similar values. They still can be two times improved by increasing the light yield at low temperature, making them similar or slightly better than those of bromide crystals.[32] Light yield stability measured from the pulse height spectra of the $(PEA)_2MAPb_2I_7$ crystal for 6 hours and the derived values of the light yield were plotted with the normalized values at the initial time as shown in Fig. S7 showing that the hygroscopicity is not as large as other iodides e.g. LaI_3: Ce^{3+}.[56] We determine the decay at high energies by investigating the γ-ray excited scintillation decay curves recorded under γ-ray excitation at 662 keV presented in Fig. 6(c) while we report the exponential fitting parameters for the decay curves in Table S4. From the decay curves in Fig. 6(c), we can immediately see that $(BA)_2PbI_4$ scintillator leads to a faster decay compared to $(PEA)_2PbI_4$ scintillator, while the decay of $(PEA)_2MAPb_2I_7$ was the slowest. The QW HOIP samples show average decay times of 190 ns and 111 ns for $(PEA)_2PbI_4$ and $(BA)_2PbI_4$, respectively. The fastest decay components of the QW HOIP crystals, were 0.5 ns and 0.4 ns for $(PEA)_2PbI_4$ and $(BA)_2PbI_4$, respectively. Such ultrafast decay components can be linked to TRPL decay curves in Figs. 4 and S4 and they were not observed in $(PEA)_2PbBr_4$ and $(BA)_2PbBr_4$.[46] The $(PEA)_2MAPb_2I_7$ perovskite show an average decay time of 112 ns and decay components of 9.3 ns (37%), 43 ns (23%), and 249 ns (39%). The fast component (< 1 ns) was not observed for $(PEA)_2MAPb_2I_7$ perovskite, due to different scintillation mechanism, dominant slow exciton and absence of free exciton emission in RL at RT. It is possible that the average lifetimes <200 ns observed were due to the higher presence of traps that lead to non-radiative processes and thus lead to a faster decay of the luminescence.[33]

▪ CONCLUSIONS

In summary, we investigated the effect of PEA and BA cation on the crystal structure, optical and scintillation properties of both QW HOIP A_2PbI_4 and $A_2MAPb_2I_7$ crystals based on the XRD analysis, absorption, PL, TRPL, temperature-dependent RL, and pulse height measurements. Based on the XRD results, we calculated the band structure and density of states using DFT analysis. From the PL measurement, we observe that A_2PbI_4 crystals exhibit green and red emission with fastest PL decay time. Overall, we observe that $(BA)_2MAPb_2I_7$ scintillator exhibit the highest mass density, smaller band gap due to the increased thickness of the inorganic slabs. We conducted temperature-dependent RL measurements to explore the effects of temperature on the scintillation properties of the perovskites, including the effect on the afterglow. We observe comparable light yields for all iodide crystals at 10 K (~10 photons/keV), while light yields at RT (between 1 and 2 photons/keV) are still much lower compared to QW HOIP bromide crystals. The biggest advantages of QW HOIP iodide scintillators compared to their bromide counterparts are shorter radiation (X- and γ-ray) absorption lengths (between 0.035 and 0.050 cm at 50 keV), faster decay time components (between 0.3 and 1.0 ns), and comparable light yields (between 7.5 and 10 photons/keV) at low temperature. Furthermore, our study on optical and scintillation properties of both A_2PbI_4 and $A_2MAPb_2I_7$ crystals provide insight for further improvements on the radiation absorptions and emission rates towards high sensitivity and fast radiation detection applications.

▪ ASSOCIATED CONTENT

The Supporting Information is available free of charge on the ACS Publications website at DOI: 10.1021/JPCC. xxxxxxx.

Rietveld refinement of crystal XRD diffractograms, absorption spectra with Elliot fits, TRPL recorded at 532 nm excitation monitoring 620 nm emission, RL spectra mapping at different temperatures, CTR results, and light yield stability of iodide-based QW HOIPS. PL and absorption spectra of $(PEA)_2PbBr_4$ and $(BA)_2PbBr_4$.

Crystallographic files (CIF)

Author Contributions

M.A.K.S.: Methodology, Formal analysis, Investigation, Writing-original draft, Writing-review & editing; **D.K., M.H.M., R.C.:** Formal analysis, Investigation, Writing-review & editing; **E.A., M.E.W., M.M., W.D., and C. D.:** Resources, Formal analysis, Writing-review & editing; **D.C.:** Conceptualization, Formal analysis, Investigation, Project administration, Funding acquisition, Writing-review & editing; **H. W.:** Resources, Writing-review & editing; **M.D.B.:** Conceptualization, Supervision, Formal analysis, Resources, Writing-review & editing, Project administration, Funding acquisition.

Notes

The authors declare no competing financial interest.

▪ ACKNOWLEDGMENTS

This work has been performed in the framework of the Crystal Clear Collaboration. D. C. acknowledges the support by the ERC Starting Grant project SUPER under grant agreement no. 101040681. M. H.M., H.W. and M. D. B. acknowledges research fund from Institut Teknologi Bandung under the "Riset ITB 2023" scheme (grant no. 308/IT1.B07.1/TA.01/2023), Singapore Ministry of Education Academic Research Fund Tier 1 (MOE Tier 1 2019-T1-002-063), and the starting fund from Lukasiewicz Research Network-PORT, respectively.

- **ABBREVIATIONS**

Hybrid organic-inorganic perovskites (HOIP), Quantum well (QW), Two-dimensional (2D), Three-dimensional (3D), Phenethylammonium (PEA), Butylammonium (BA), Room temperature (RT), X-ray diffraction (XRD), Density of states (DOS), Density functional theory (DFT), Photoluminescence (PL), Time-resolved PL (TRPL), Radioluminescence (RL), Thermoluminescence (TL), Coincidence time resolution (CTR).

- **REFERENCES**

(1) A. Kojima; K. Teshima; Y. Shirai; Miyasaka, T. Organometal halide perovskites as visible-light sensitizers for photovoltaic cells. *J. Am. Chem. Soc.* **2009**, *131* (17), 6050-6051. DOI: 10.1021/ja809598r.
(2) P. Li; Y. Zhang; C. Liang; G. Xing; X. Liu; F. Li; X. Liu; X. Hu; G. Shao; Song, Y. Phase pure 2D perovskite for high-performance 2D-3D heterostructured perovskite solar cells. *Adv. Mater.* **2018**, *30*, 1805323. DOI: 10.1002/adma.201805323.
(3) C. T. Zuo; H. J. Bolink; H. W. Han; J. S. Huang; D. Cahen; Ding, L. M. Advances in perovskite solar cells. *Adv. Sci.* **2016**, *3*, 1500324. DOI: 10.1002/advs.201500324.
(4) H. -S. Kim; A. Hagfeldt; Park, N.-G. Morphological and compositional progress in halide perovskite solar cells. *Chem. Commun.* **2019**, *55*, 1192-1200. DOI: 10.1039/C8CC08653B.
(5) P. Wang; Y. Wu; B. Cai; Q. Ma; X. Zheng; Zhang, W. H. Solution-processable perovskite solar cells toward commercialization: progress and challenges. *Adv. Funct. Mater.* **2019**, *29*, 1807661. DOI: 10.1002/adfm.201807661.
(6) X. Chin, D. C., J. Yin, A. Bruno, C. Soci. Lead iodide perovskite light-emitting field-effect transistor. *Nat. Commun.* **2015**, *6*, 7383. DOI: 10.1038/ncomms8383.
(7) I. C. Smith, E. T. H., D. Solis-Ibarra, M. D. McGehee and; Karunadasa, H. I. A layered hybrid perovskite solar-cell absorber with enhanced moisture stability. *Angew. Chem. Int. Ed.* **2014**, *53* (42), 11232-11235. DOI: 10.1002/anie.201406466.
(8) L. Mao; Y. Wu; C. C. Stoumpos; M. R. Wasielewski; Kanatzidis, M. G. White-light emission and structural distortion in new corrugated two-dimensional lead bromide perovskites. *J. Am. Chem. Soc.* **2017**, *139* (14), 5210-5215. DOI: 10.1021/jacs.7b01312.
(9) J. -P. Correa-Baena; A. Abate; M. Saliba; W. Tress; T. J. Jacobson; M. Grätzel; Hagfeldt, A. The rapid evolution of highly efficient perovskite solar cells. *Energy Environ. Sci.* **2017**, *10*, 710-727. DOI: 10.1039/C6EE03397K.
(10) H. Tsai; W. Nie; J.-C. Blancon; C. C. Stoumpos; C. M. M. Soe; J. Yoo; J. Crochet; S. Tretiak; J. Even; A. Sadhanala; et al. Stable light-emitting diodes using phase-pure ruddlesden–popper layered perovskites. *Adv. Mater.* **2018**, *30*, 1704217. DOI: 10.1002/adma.201704217.
(11) B. R. Sutherland; Sargent, E. H. Perovskite photonic sources. *Nat. Photonics* **2016**, *10*, 295-302. DOI: 10.1038/nphoton.2016.62.
(12) H. Wang; Kim, D. H. Perovskite-based photodetectors: materials and devices. *Chem. Soc. Rev.* **2017**, *46*, 5204-5236. DOI: 10.1039/C6CS00896H.
(13) Y. Fu; H. Zhu; J. Chen; M. P. Hautzinger; X. -Y. Zhu; Jin, S. Metal halide perovskite nanostructures for optoelectronic applications and the study of physical properties. *Nat. Rev. Mater.* **2019**, *4*, 169-188. DOI: 10.1038/s41578-019-0080-9.

(14) A. Xie; C. Hettiarachchi; F. Maddalena; M. E. Witkowski; M. Makowski; W. Drozdowski; Arramel; A. T. S. Wee; S. V. Springham; P. Q. Vuong; et al. Lithium-doped two-dimensional perovskite scintillator for wide-range radiation detection. *Commun. Mater.* **2020**, *1* (1), 37. DOI: 10.1038/s43246-020-0038-x.
(15) S. Kumar; J. Jagielski; S. Yakunin; P. Rice; Y. -C. Chiu; M. Wang; G. Nedelcu; Y. Kim; S. Lin; E. J. G. Santos; et al. Efficient blue electroluminescence using quantum-confined two-dimensional perovskites. *ACS Nano* **2016**, *10* (10), 9720-9729. DOI: 10.1021/acsnano.6b05775.
(16) A. Xie; F. Maddalena; M. E. Witkowski; M. Makowski; B. Mahler; W. Drozdowski; S. V. Springham; P. Coquet; C. Dujardin; M. D. Birowosuto; et al. Library of two-dimensional hybrid lead halide perovskite scintillator crystals. *Chem. Mater.* **2020**, *32* (19), 8530-8539. DOI: 10.1021/acs.chemmater.0c02789.
(17) A. Wibowo; Md A. K. Sheikh; L. J. Diguna, M. B. A.; M. A. Marsudi; Arramel; S. Zeng; W. L. Jie; Birowosuto, M. D. Development and challenges in perovskite scintillators for high resolution imaging, and timing applications. *Commun. Mater.* **2023**, *4* (21). DOI: 10.1038/s43246-023-00348-5.
(18) Y. Yang; F. Gao; S. Gao; Wei, S.-H. Origin of the stability of two-dimensional perovskites: a first-principles study. *J. Mater. Chem. A* **2018**, *6*, 14949-14955. DOI: 10.1039/C8TA01496E.
(19) M. D. Birowosuto; D. Cortecchia; W. Drozdowski; K. Brylew; W. Lachmanski; A. Bruno; Soci, C. X-ray scintillation in lead halide perovskite crystals. *Sci. Rep.* **2016**, *6* (1), 37254. DOI: 10.1038/srep37254.
(20) F. Maddalena; L. Tjahjana; A. Xie; Arramel; S. Zeng; H. Wang; P. Coquet; W. Drozdowski; C. Dujardin; C. Dang; et al. Inorganic, organic, and perovskite halides with nanotechnology for high–light yield X- and γ-ray scintillators. *Crystals* **2019**, *9* (88). DOI: 10.3390/cryst9020088.
(21) N. Kawano; M. Koshimizu; A. Horiai; F. Nishikido; R. Haruki; S. Kishimoto; K. Shibuya; Y. Fujimoto; T. Yanagida; Asai, K. Effect of organic moieties on the scintillation properties of organic–inorganic layered perovskite-type compounds. *Jpn. J. Appl. Phys.* **2016**, *55*, 110309. DOI: 10.7567/JJAP.55.110309.
(22) K. Shibuya; M. Koshimizu; Y. Takeoka; K. Asai. Scintillation properties of $(C_6H_{13}NH_3)_2PbI_4$: exciton luminescence of an organic/inorganic multiple quantum well structure compound induced by 2.0 MeV protons. *Nucl. Instrum. Methods Phys. Res., Sect. B* **2002**, *194* (2), 207-212. DOI: 10.1016/S0168-583X(02)00671-7.
(23) S. Kishimoto; K. Shibuya; F. Nishikido; M. Koshimizu; R. Haruki; Yoda, Y. Subnanosecond time resolved X-ray measurements using an organic-inorganic perovskite scintillator. *Appl. Phys. Lett.* **2018**, *93* (26), 261901. DOI: 10.1063/1.3059562.
(24) C. Dujardin; E. Auffray; E. Bourret-Courchesne; P. Dorenbos; P. Lecoq; M. Nikl; A. N. Vasil'ev; A. Yoshikawa; Zhu, R. Y. Needs, trends, and advances in inorganic scintillators. *IEEE Trans. Nucl. Sci.* **2018**, *65* (8), 1977-1997. DOI: 10.1109/TNS.2018.2840160.
(25) H. Tsai, W. N., J. C. Blancon,; C. C. Stoumpos, R. A., B. Harutyunyan, A. J.; Neukirch, R. V., J. J. Crochet, S. Tretiak, L. Pedesseau,; J. Even, M. A. A., G. Gupta, P. M. Ajayan, M. J. Bedzyk,; Mohite, M. G. K. a. A. D. High-efficiency two-dimensional Ruddlesden–Popper perovskite solar cells. *Nature* **2016**, *536*, 312-316. DOI: 10.1038/nature18306.
(26) Z. Xiao, W. M., J. Wang, D. B. Mitzi, Y. Yan. Searching for promising new perovskite-based photovoltaic absorbers: the importance of electronic dimensionality. *Mater. Horiz.* **2017**, *4*, 206-216. DOI: 10.1039/C6MH00519E.
(27) C. M. M. Soe, C. C. S., M. Kepenekian, B. Traoré, H. Tsai, W. Nie, B. Wang, C. Katan, R. Seshadri, A. D. Mohite, J. Even, T. J. Marks, M. G. Kanatzidis. New type of 2D perovskites with

alternating cations in the interlayer space, $(C(NH_2)_3)(CH_3NH_3)_nPb_nI_{3n+1}$: structure, properties, and photovoltaic performance. *J. Am. Chem. Soc.* **2017**, *139* (45), 16297-16309. DOI: 10.1021/jacs.7b09096.

(28) C. R. Kagan, D. B. M. a. C. D. D. Organic-inorganic hybrid materials as semiconducting channels in thin-film field-effect transistors. *Science* **1999**, *286*, 945. DOI: 10.1126/science.286.5441.945.

(29) X. X. Wu, M. T. T., D. Niesner, H. M. Zhu, Z. Norman,; J. S. Owen, O. Y., B. J. Kudisch and X. Y. Zhu Trap states in lead iodide perovskites. *J. Am. Chem. Soc.* **2015**, *137* (5), 2089-2096. DOI: 10.1021/ja512833n.

(30) M. Yuan, L. Q., R. Comin, G. Walters, R. Sabatini, O. Voznyy,; S. Hoogland, Y. Z., E. M. Beauregard, P. Kanjanaboos, Z. Lu,; Sargent, D. H. K. a. E. H. Perovskite energy funnels for efficient light-emitting diodes. *Nat. Nanotechnol.* **2016**, *11*, 872. DOI: 10.1038/nnano.2016.110.

(31) J. Wong; Yang, K. 2D hybrid halide perovskites: synthesis, properties, and applications. *Sol. RRL* **2021**, *5* (1), 2000395. DOI: 10.1002/solr.202000395.

(32) D. Kowal; M. Makowski; M. E. Witkowski; R. Cala'; Md A. K. Sheikh; M. H. Mahyuddin; E. Auffray; W. Drozdowski; D. Cortecchia; Birowosuto, M. D. PEA_2PbI_4: Fast two-dimensional lead iodide perovskite scintillator with green and red emission. *Mater. Today Chem.* **2023**, *29* (101455). DOI: 10.1016/j.mtchem.2023.101455.

(33) F. Maddalena; A. Xie; Arramel; M. E. Witkowski; M. Makowski; B. Mahler; W. Drozdowski; T. Mariyappan; S. V. Springham; P. Coquet; et al. Effect of commensurate lithium doping on the scintillation of two-dimensional perovskite crystals. *J. Mater. Chem. C* **2021**, *9*, 2504-2512. DOI: 10.1039/d0tc05647b.

(34) W. Kohn; Sham, L. J. Self-consistent equations including exchange and correlation effects. *Phys. Rev.* **1965**, *140*, A1133-A1138. DOI: 10.1103/PhysRev.140.A1133.

(35) G. Kresse; Furthmüller, J. Efficiency of ab-initio total energy calculations for metals and semiconductors using a plane-wave basis set. *Comput. Mater. Sci.* **1996**, *6* (1), 15-50. DOI: 10.1016/0927-0256(96)00008-0.

(36) P. E. Blöchl. Projector augmented-wave method. *Phys. Rev. B* **1994**, *50*, 17953-17979. DOI: 10.1103/PhysRevB.50.17953.

(37) C. C. Stoumpos; D. H. Cao; D. J. Clark; J. Young; J. M. Rondinelli; J. I. Jang; J. T. Hupp; Kanatzidis, M. G. Ruddlesden-popper hybrid lead iodide perovskite 2D homologous semiconductors. *Chem. Mater.* **2016**, *28*, 2852-2867. DOI: 10.1021/acs.chemmater.6b00847.

(38) J. Yin; R. Naphade; L. G. Arzaluz; J. -L. Brédas; O. M. Bakr; Mohammed, O. M. Modulation of broadband emissions in two dimensional ⟨100⟩-oriented ruddlesden-popper hybrid perovskites. *ACS Energy Lett.* **2020**, *5*, 2149-2155. DOI: 10.1021/acsenergylett.0c01047.

(39) K. -Z. Du; Q. Tu; X. Zhang; Q. Han; J. Liu; S. Zauscher; Mitzi, D. B. Two-dimensional lead(ii) halide-based hybrid perovskites templated by acene alkylamines: crystal structures, optical properties, and piezoelectricity. *Inorg. Chem.* **2017**, *56*, 9291-9302. DOI: 10.1021/acs.inorgchem.7b01094.

(40) J. Song; Y. Dang; X . L. Liua; Tao, X. Layered hybrid lead perovskite single crystals: phase transformations and tunable optical properties. *CrystEngComm* **2020**, *22*, 6310-6315. DOI: 10.1039/d0ce00753f.

(41) J. Calabrese, N. L. J., R. L. Harlow, N. Herron, D. L. Thorn, Y. Wang. Preparation and characterization of layered lead halide compounds. *J. Am. Chem. Soc.* **1991**, *113* (6), 2328-2330. DOI: 10.1021/ja00006a076.

(42) D. B. Mitzi. Synthesis, crystal structure, and optical and thermal properties of $(C_4H_9NH_3)_2MI_4$ (M = Ge, Sn, Pb). *Chem. Mater.* **1996**, *8* (3), 791-800. DOI: 10.1021/cm9505097.
(43) D. G. Billing; Lemmerer, A. Synthesis, characterization and phase transitions in the inorganic-organic layered perovskite-type hybrids $[(C_nH_{2n+1}NH_3)_2PbI_4]$, n = 4, 5 and 6. *Acta Crystallogr., Sect. B: Struct. Sci.* **2007**, *63*, 735-747. DOI: 10.1107/S0108768107031758.
(44) *NIST X-ray attenuation calculatior*. https://physics.nist.gov/PhysRefData/FFast/html/form.html (accessed 20th January 2023).
(45) Md A. K. Sheikh; D. Kowal; M. H. Mahyuddin; D. Onggo; F. Maddalena; C. Dang; R. Cala'; E. Auffray; M. E. Witkowski; M. Makowski; et al. Solution-processable A_2XY_4 (A=PEA, BA, X= Pb, Sn, Cu, Mn; Y=Cl, Br, I) crystals for high light yield and ultrafast scintillators. *IEEE Trans. Nucl. Sci.* **2022, (Under review)**.
(46) F. Maddalena; M. H. Mahyuddin; D. Kowal; M. E. Witkowski; M. Makowski; Md A. K. Sheikh; S. Mahato; R. Je̜drzejewski; W. Drozdowski; C. Dujardin; et al. Lattice expansion in rubidium doped hybrid organic-inorganic perovskite crystals resulting smaller-bandgap and higher-light-yield scintillators. *Inorg. Chem.* **2023 (Under review)**.
(47) Y. Yuan; X. -F. Liu; X. Ma; X. Wang; X. Li; J. Xiao; X. Li; H. -L. Zhang; Wang, L. Large band gap narrowing and prolonged carrier lifetime of $(C_4H_9NH_3)_2PbI_4$ under high pressure. *Adv. Sci.* **2019**, *6*, 1900240. DOI: 10.1002/advs.201900240.
(48) W. Peng, J. Y., K.-T. Ho, O. Ouellette, M. D. Bastiani, B.; Murali, O. E. T., C. Shen, X. Miao, J. Pan, E. Alarousu, J.-H.; He, B. S. O., O. F. Mohammed, E. Sargent and O. M. Bakr Ultralow delf-doping in two-dimensional hybrid perovskite single crystals. *Nano Lett.* **2017**, *17*, 4759. DOI: 10.1021/acs.nanolett.7b01475.
(49) R. J. Elliott. Theory of the effect of spin-orbit coupling on magnetic resonance in some semiconductors. *Phys. Rev.* **1954**, *96* (2), 266-279. DOI: 10.1103/PhysRev.96.266.
(50) J.-C. Blancon; H. Tsai; W. Nie; C. C. Stoumpos; L. Pedesseau; C. Katan; M. Kepenekian; C. M. M. Soe; K. Appavoo; M. Y. Sfeir; et al. Extremely efficient internal exciton dissociation through edge states in layered 2D perovskite. *Science* **2017**, *355* (6331), 1288-1292. DOI: 10.1126/science.aal4211
(51) S. Kahmann; D. Meggiolaro; L. Gregori; E. K. Tekelenburg; M. Pitaro; S. D. Stranks; F. D. Angelis; Loi, M. A. The origin of broad emission in ⟨100⟩ two dimensional perovskites: extrinsic vs intrinsic processes. *ACS Energy Lett.* **2022**, *7*, 4232-4241. DOI: 10.1021/acsenergylett.2c02123.
(52) L. J. Diguna; L. Jonathan; M. H. Mahyuddin; Arramel; F. Maddalena; I. Mulyani; D. Onggo; A. Bachiri; M. E. Witkowski; M. Makowski; et al. BA_2XBr_4 (X = Pb, Cu, Sn): from lead to lead-free halide perovskite scintillators. *Mater. Adv.* **2022**, *3* (12), 5087-5095. DOI: 10.1039/D2MA00258B.
(53) H. Hardhienata; F. Ahmad; M. Aminah; D. Onggo; L. J. Diguna; M. D. Birowosuto; M. E. Witkowski; M. Makowski; Drozdowski, W. Optical and X–ray scintillation properties of X_2MnCl_4 (X= PEA, PPA) perovskite crystals. *J. Phys. D: Appl. Phys.* **2020**, *53* (45), 455303.
(54) G. Gordillo; C. A. Otálora; Ramirez, A. A. A study of trap and recombination centers in $MAPbI_3$ perovskites. *Phys. Chem. Chem. Phys.* **2016**, *18*, 32862-32867. DOI: 10.1039/C6CP06261J.
(55) W. Zhai; C. Ge; X. Fang; K. Zhang; C. Tian; K. Yuan; S. Sun; Y. Li; W. Chen; Ran, G. Acetone vapour-assisted growth of 2D single-crystalline organic lead halide perovskite

microplates and their temperature-enhanced photoluminescence. *RSC Adv.* **2018**, *8*, 14527-14531. DOI: 10.1039/C8RA00583D.

(56) A. Bessiere, P. D., C. W. E. van Eijk, K. W. Krämer, H. U. Güdel, C. de M. Donega, A. Meijerink. Luminescence and scintillation properties of the small band gap compound $LaI_3:Ce^{3+}$. *Nucl. Instrum. Methods Phys. Res., Sect. A* **2005**, *537* (1-2), 22-26. DOI: 10.1016/j.nima.2004.07.224.

(57) J. J. V. Blaaderen; F. Maddalena; C. Dang; M. D. Birowosuto; Dorenbos, P. Temperature dependent scintillation properties and mechanisms of $(PEA)_2PbBr_4$ single crystals. *J. Mater. Chem. C* **2022**, *10*, 11598-11606. DOI: 10.1039/D2TC01483A.

(58) R. Cala'; I. Frank; F. Pagano; F. Maddalena; C. Dang; M. D. Birowosuto; Auffray, E. Sub-100-picosecond time resolution from undoped and Li-doped two-dimensional perovskite scintillators. *Appl. Phys. Lett.* **2022**, *120* (24), 241901. DOI: 10.1063/5.0093606.

TOC Graphic